



Universiteit
Leiden
The Netherlands

Fountain-driven gas accretion feeding star formation over the disc of NGC 2403

Li, A.; Fraternali, F.; Marasco, A.; Trager, S.C.; Pezzulli, G.; Mancera Piña, P.E.; Verheijen, M.A.W.

Citation

Li, A., Fraternali, F., Marasco, A., Trager, S. C., Pezzulli, G., Mancera Piña, P. E., & Verheijen, M. A. W. (2023). Fountain-driven gas accretion feeding star formation over the disc of NGC 2403. *Monthly Notices Of The Royal Astronomical Society*, 520(1), 147-160. doi:10.1093/mnras/stad129

Version: Publisher's Version
License: [Creative Commons CC BY 4.0 license](https://creativecommons.org/licenses/by/4.0/)
Downloaded from: <https://hdl.handle.net/1887/3719094>

Note: To cite this publication please use the final published version (if applicable).

Fountain-driven gas accretion feeding star formation over the disc of NGC 2403

Anqi Li ¹★, Filippo Fraternali ¹★, Antonino Marasco ^{2,3}, Scott C. Trager ¹, Gabriele Pezzulli ¹,
Pavel E. Mancera Piña ^{1,4,5} and Marc A. W. Verheijen ¹

¹*Kapteyn Astronomical Institute, University of Groningen, Landleven 12, 9747 AD Groningen, The Netherlands*

²*INAF-Osservatorio Astronomico di Padova, Vicolo dell'Osservatorio 5, I-35122 Padova, Italy*

³*INAF-Osservatorio Astrofisico di Arcetri, Largo Enrico Fermi, 550125 Firenze, Italy*

⁴*ASTRON, Netherlands Institute for Radio Astronomy, Postbus 2, NL-7900 AA Dwingeloo, The Netherlands*

⁵*Leiden Observatory, Leiden University, P.O. Box 9513, NL-2300 AA Leiden, The Netherlands*

Accepted 2022 December 31. Received 2022 November 23; in original form 2022 September 13

ABSTRACT

We use a dynamical model of galactic fountain to study the neutral extraplanar gas (EPG) in the nearby spiral galaxy NGC 2403. We have modelled the EPG as a combination of material ejected from the disc by stellar feedback (i.e. galactic fountain) and gas accreting from the inner circumgalactic medium (CGM). This accretion is expected to occur because of cooling/condensation of the hot CGM (corona) triggered by the fountain. Our dynamical model reproduces the distribution and kinematics of the EPG HI emission in NGC 2403 remarkably well and suggests a total EPG mass of $4.7^{+1.2}_{-0.9} \times 10^8 M_{\odot}$, with a typical scale height of around 1 kpc and a vertical gradient of the rotation velocity of $-10.0 \pm 2.7 \text{ km s}^{-1} \text{ kpc}^{-1}$. The best-fitting model requires a characteristic outflow velocity of $50 \pm 10 \text{ km s}^{-1}$. The outflowing gas starts out mostly ionized and only becomes neutral later in the trajectory. The accretion rate from the condensation of the inner hot CGM inferred by the model is $0.8 M_{\odot} \text{ yr}^{-1}$, approximately equal to the star-formation rate in this galaxy ($0.6 M_{\odot} \text{ yr}^{-1}$). We show that the accretion profile, which peaks at a radius of about 4.5 kpc, predicts a disc growth rate compatible with the observed value. Our results indicate that fountain-driven corona condensation is a likely mechanism to sustain star formation, as well as the disc inside-out growth in local disc galaxies.

Key words: ISM: kinematics and dynamics – ISM: structure – galaxies: evolution – galaxies: haloes – galaxies: ISM – galaxies: intergalactic medium.

1 INTRODUCTION

Nearby spiral galaxies have been forming stars, across their lifetimes, at an approximately constant or gently declining rate, despite the fact that the gas in their interstellar medium (ISM) would, without replenishment, be consumed in a few Gyr (Aumer & Binney 2009; Tacconi et al. 2018). An external gas reservoir is therefore needed from which galaxies accrete gas at a rate compatible with their SFR (e.g. Fraternali & Tomassetti 2012). Gas-rich mergers are not providing a sufficient contribution, at least in the local Universe (Sancisi et al. 2008; Di Teodoro & Fraternali 2014). Therefore the majority of the accretion must come from the diffuse gas that resides outside galaxies.

The multiphase circumgalactic medium (CGM) is expected to host a significant fraction of the baryons associated with dark matter halos in normal spiral galaxies (e.g. Crain et al. 2007; Tumlinson et al. 2011; Li et al. 2018), which makes it the most probable gas reservoir eligible for accretion. A prominent component of the CGM is hot gas ($T \sim 10^6\text{--}7$ K) in the form of a diffuse ‘corona’ at nearly the virial temperature and in nearly hydrostatic equilibrium with the dark matter potential (e.g. White & Frenk 1991; Pezzulli,

Fraternali & Binney 2017). Galactic coronae are thought to surround galaxies and to be extended to their virial radii (Fukugita & Peebles 2006; Faerman, Sternberg & McKee 2020). Direct detection of the hot coronae in X-rays is limited to the innermost few tens of kpc in massive galaxies with stellar mass beyond $10^{11} M_{\odot}$ (e.g. Anderson & Bregman 2011; Walker, Bagchi & Fabian 2015; Anderson, Churazov & Bregman 2016), while indirect evidence of their presence extends further (e.g. Gatto et al. 2013; Putman et al. 2021). Cool CGM ($T \sim 10^4$ K) gas has also been detected, mostly in absorption along quasar sightlines, in several studies (e.g. Heckman et al. 2017; Rubin et al. 2018; Zahedy et al. 2019). Like the hot corona, also these cool absorbers extend to large distances (up to and sometimes beyond the virial radius) and their origin and fate remain debated (Rubin et al. 2010; Schroetter et al. 2019; Pointon et al. 2019; Afruni, Fraternali & Pezzulli 2021).

Although gas accretion from the CGM is crucial to feed star formation (Hopkins, McClure-Griffiths & Gaensler 2008; Sancisi et al. 2008; Kereš et al. 2009), how precisely it takes place is still unknown. One possible accretion scenario is that cold filaments reach the outer disc (Lagos et al. 2017; El-Badry et al. 2018; Trapp et al. 2022) and are transported into the inner star-forming regions via radial motions, although Di Teodoro & Peek (2021) found that radial inflows in nearby galaxies alone could not sustain the star-formation rates. Other possible mechanisms include cold gas filaments directly

* E-mail: li@astro.rug.nl (AL); fraternali@astro.rug.nl (FF)

feeding the inner regions of a galaxy or the cooling of the hot corona (Kereš et al. 2005; Nelson et al. 2013; Voit et al. 2015). The spontaneous cooling of the corona via thermal instability is still under debate as a number of works suggest that the combination of buoyancy and thermal conduction can suppress the growth of thermal perturbations (e.g. Binney, Nipoti & Fraternali 2009; Nipoti 2010; Joung, Bryan & Putman 2012). Some authors have proposed that coronal condensation could be triggered by the ejection of gas from the disc due to stellar feedback, such as in supernova-powered superbubbles (Fraternali 2017, and references therein). In this scenario, the cooling of the hot gas is due to the mixing with the cool gas ejected from the disc and occurs within the fountain cycle. This process can be detected in high-quality data as it leaves a mark in the kinematics of the ejected disc gas (Fraternali & Binney 2008; Marasco, Fraternali & Binney 2012).

To gain insight into the gas exchange processes between the disc and the inner hot CGM, one must focus on the disc-halo interface region. Deep HI observations have shown that disc galaxies, including the Milky Way, are surrounded by a neutral gas layer extending up to a few kpc from their disc planes (e.g. Wakker 2001; Sancisi et al. 2008; Hess et al. 2009; Marasco & Fraternali 2011). This gas layer, known as extraplanar gas (EPG), is nearly ubiquitous in late-type galaxies and has a mass of 10–30 per cent of the mass of the HI in the disc (Marasco et al. 2019). The kinematics of the EPG is primarily characterized by differential rotation, similar to the disc, but with a negative rotational gradient (lag) ranging from -10 to $-20 \text{ km s}^{-1} \text{ kpc}^{-1}$ in the vertical direction (e.g. Oosterloo, Fraternali & Sancisi 2007; Zschaechner et al. 2011). Non-circular motions, especially large-scale inflows are also often found (e.g. Fraternali et al. 2002; Barbieri et al. 2005; Marasco et al. 2019). Ionized EPG has also been detected, both in the Milky Way (Dettmar 1990; Lehner et al. 2012, 2022) and in several other galaxies (Heald et al. 2005; Levy et al. 2019), with similar kinematics as the neutral EPG (Kamphuis et al. 2007; Li et al. 2021; Marasco et al. 2022).

The similarity between EPG and disc kinematics strongly suggests that EPG originates mostly from the disc, very likely pushed out of the plane due to stellar feedback and pulled back by gravity. This phenomenon is also known as ‘galactic fountain’ (Shapiro & Field 1976; Bregman 1980). Fraternali & Binney (2006, hereafter FB06) built ballistic models of galactic fountain flows, which successfully reproduced many of the observed properties of the EPG in the two nearby galaxies NGC 891 and NGC 2403. It is worth noticing that ballistic models also describe very well the properties of the warm gas (neutral and ionized) in the hydrodynamical TIGRESS simulations (Vijayan et al. 2020). However, a pure fountain model failed to reproduce the net inward flow (instead, an outward flow was predicted) and underestimated the rotation lag compared to the observed EPG in NGC 891 and NGC 2403. Fraternali & Binney (2008, hereafter FB08) mitigated these issues by introducing an external factor that could lower the angular momentum of fountain gas: accretion from the ambient gas. Although initially introduced to reproduce the kinematics of the EPG, the net inflow rate derived from this model turned out to be consistent with the SFR of the two galaxies, suggesting that the accretion triggered by the fountain cycle could be a viable mechanism to maintain the star-formation activity.

An unsolved issue of the earlier fountain-driven accretion scenario was the source of the accretion. This has been explored by Marinacci et al. (2010) with hydrodynamical simulations. Their simulations of fountain gas clouds interacting with the hot corona indicated that the corona was a possible accretion source. During the interaction process, part of the fountain gas is stripped and mixed with the hot gas. The mixture has a typical temperature of $T \sim 10^5 \text{ K}$, where the

cooling function peaks, and also higher metallicity and density than the hot corona. As a consequence, the cooling time is reduced to a value shorter than the travel time of fountain gas. This result has been confirmed by other simulations with increasing levels of complexity (Armillotta, Fraternali & Marinacci 2016; Gronke & Oh 2018; Kooij, Grønnow & Fraternali 2021). Some studies have upgraded the approach of FB08, taking into account the results of hydrodynamical simulations, using physical properties of the EPG and the hot corona as adjustable parameters, and managed to reproduce the phase-space distribution of both neutral and ionized EPG in the disc-halo interface of Milky Way remarkably well (Marasco, Marinacci & Fraternali 2013; Fraternali et al. 2013; Marasco et al. 2012, hereafter M12). The best-fitting model predicted a net inflow rate which is consistent with the SFR of the Milky Way.

The aforementioned studies strongly suggest that fountain-driven accretion takes place in the Milky Way and provides a promising explanation for how galaxies like our own can sustain their star formation with time. However, so far the Milky Way remains the only galaxy for which a state-of-the-art model of the galactic fountain has been applied to the observations using a parametric fitting methodology, which is required to robustly characterize the fountain flow and to quantify the properties of the accreting gas. The earlier models in FB08 did not statistically explore the parameter space, and furthermore, did not include the condensation of the corona, since hydrodynamical simulations were not available by then. In this paper, we revisit this by applying our state-of-the-art fountain model to NGC 2403, using high-quality HI data (with a beam size of $30'' \times 29''$ and an rms-noise of $0.19 \text{ mJy beam}^{-1}$) from Fraternali et al. (2002), which were later included in the HALOGAS survey (Heald et al. 2011). Table 1 summarizes the main physical properties of NGC 2403.

In Section 2, we provide a description of our dynamical model of the galactic fountain. In Section 3, we discuss the customization we have made to implement the model for the case of NGC 2403. In Section 4, we present the modelling results. In Section 5, we discuss the reliability of our results and possible implications. We summarize our analysis in Section 6.

2 THE MODEL

In this Section, we describe the main ingredients of our model and discuss its main free parameters. Further details can be found in FB06, FB08, and M12. We consider two different types of models: a ‘pure fountain’ ballistic model and a ‘fountain + corona accretion’ model which takes the interaction of fountain clouds with the hot coronal gas into consideration. In both scenarios, the models have a quasi-stationary state and are axisymmetric. The neutral EPG in the disc-halo interface region is modelled as a collection of clouds that are ejected from the disc at different radii with a given distribution of initial velocities and angles, and whose orbits are then integrated in time and followed across the halo region until they return to the disc.

Since galactic fountains are powered by stellar feedback, we assume that the amount of gas ejected from each location in the disc is proportional to the SFR surface density at that radius. In practice, we incorporate this assumption by assigning, to each of our modelled clouds, a weight proportional to the SFR surface density at the ejection radius. This weight is then factored in when creating the mock data cube to be compared with observations (see also further explanations below).

In our pure fountain ballistic models, the trajectories of the fountain clouds are integrated using a numerical approximation of the galaxy gravitational potential, derived as described in Section 3.1.

Table 1. Galaxy properties.

Galaxy name	RA	Declination	PA	Inclination	Distance	Hubble Type	M_B	M_*	$M_{\text{HI, EPG}}$	SFR
(1)	(2)	(3)	[$^\circ$]	[$^\circ$]	[Mpc]	(7)	(8)	[$10^8 M_\odot$]	[$10^8 M_\odot$]	[$M_\odot \text{yr}^{-1}$]
(1)	(2)	(3)	(4)	(5)	(6)	(7)	(8)	(9)	(10)	(11)
NGC 2403	07 ^h 36 ^m 51 ^s .4	+ 65° 36′ 09″.2	124.6	62.5	3.2	SACd	−19.68	71.9	5.9	0.6

Columns: (1) Galaxy name. (2)–(3): Coordinates (J2000). (4)–(5): Position-angle and inclination. (6) Distance. (7) Hubble type. (8) Absolute magnitude in the *B*-band. (9) Stellar mass (see Pezzulli et al. 2015). (10) Total mass of H I EPG. (11) Total star-formation rate of the galaxy. Values in this table are taken from Marasco et al. (2019) unless otherwise mentioned.

For fountain + corona accretion models, hydrodynamical forces due to the interaction between the clouds and the hot corona are parametrized in simple forms described in Section 2.3.

The positions and velocities of the clouds along their orbits are recorded at each time-step (0.3 Myr), projected along the line-of-sight of the observer, weighted by the local SFR surface density at the ejection radius and transferred into a synthetic data cube, which is then adapted to a specific galaxy (NGC 2403 in our case) by assuming a distance, inclination (INCL), and position angle (PA), and using the same observational setup (beam shape, spectral resolution, pixel size, etc.) of the data under consideration. The outcome of the dynamical model is therefore a synthetic data cube which can be directly compared with the observational H I data of our target galaxy.

Construction of the model involves several parameters but we will focus preferentially on three (for pure fountain models) or four (only for fountain + corona accretion models) that regulate the initial outflow speed of the clouds, their neutral gas fraction, the EPG total mass and, for models that include interaction with the corona, an additional parameter that regulates the condensation efficiency. Later we discuss these parameters in detail. Other ingredients are fixed by the observations, in particular the galaxy potential (which affects the trajectory of the cloud) and the SFR surface-density profile (which regulates the ejection rate), as described in Section 3.

2.1 Outflow velocity

Fountain clouds are initially located within the galaxy disc and rotate at the circular speed set by our gravitational potential.¹ Each cloud receives a ‘kick’ with a velocity v_k at certain angles θ , which is defined as the angle between the velocity vector and the direction normal to the disc plane. The probability distribution of the ejection as a function of v_k and θ (assuming a uniform probability in the azimuthal direction) follows FB06 and is given by

$$\mathcal{P}(v_k, \theta) \propto \exp\left(-\frac{v_k^2}{2h_v^2 \cos^{2\Gamma} \theta}\right), \quad (1)$$

where h_v is the characteristic velocity, and Γ determines the level of collimation of the ejected clouds. Larger values of h_v increase the probability that a cloud is kicked at high speed. The larger Γ , the more collimated the ejection. FB06 have tested models with different values for Γ and found that more collimated ejections agree better with the data. We have therefore fixed $\Gamma = 10$ (highly collimated).

The outflow velocity of a cloud affects the maximum height and the trajectory of the orbit and therefore influences the final model. We, therefore, let the characteristic velocity h_v be a free parameter with

¹They also feature an additional velocity component, with an amplitude randomly extracted from a Gaussian distribution with rms of 8 km s^{-1} and a random (isotropic) direction, to simulate the typical velocity dispersion of the neutral ISM (Iorio et al. 2017; Bacchini et al. 2019; Mancera Piña et al. 2021).

a flat prior in the range $40\text{--}100 \text{ km s}^{-1}$. This range covers the typical characteristic ejection speeds of the warm gas in high-resolution hydrodynamical simulations of galactic fountains (Kim & Ostriker 2018). It also agrees with theoretical estimates of the typical blow-out speed of individual superbubbles (e.g. Mac Low & McCray 1988; Keller et al. 2014).

2.2 Phase change

Previous studies have found that the neutral EPG in some spiral galaxies (including the Milky Way) shows a tentative preference for vertical inflow (e.g. Marasco et al. 2019; French et al. 2021), which can be interpreted as due to a change of phase during the fountain cloud orbit: gas is largely ionized when ejected from the star-forming region of the disc but later recombines and becomes visible in H I at some point during its trajectory. To account for this effect in our model, we assume that a cloud is only visible in the H I phase when

$$v_z(t) < v_{z,0}(1 - f_{\text{ion}}), \quad (2)$$

where v_z is the vertical velocity (i.e. in the direction perpendicular to the disc) of the cloud, $v_{z,0}$ is the vertical component of the initial outflow velocity and f_{ion} is the ionization fraction parameter, which we set as a free parameter with a flat prior and varies from zero to one. When f_{ion} equals zero, the cloud is visible in the whole orbit, while when f_{ion} equals one, the cloud is only visible when $v_z < 0$ (i.e. the descending stage).

2.3 Interaction with the corona

In our model, the hot corona is modelled as a smooth, volume-filling gas layer that rotates at a lower speed than the disc, which is justified on both observational (Hodges-Kluck, Miller & Bregman 2016) and theoretical (Pezzulli et al. 2017) grounds. We assume that the corona maintains a temperature of $\sim 10^6 \text{ K}$, which implicitly implies some heating by either supernova feedback (e.g. Stinson et al. 2013) or active galactic nucleus feedback (for galaxies with ongoing AGN activities; e.g. Ciotti & Ostriker 2012). The condensation and accretion of the hot corona is triggered by the cool ($T \sim 10^4 \text{ K}$) fountain clouds ejected from the disc, which mix efficiently with the former and produce a mixture at $T \sim 10^5 \text{ K}$, dramatically reducing the cooling time of the hot corona. The earlier processes have been investigated in the hydrodynamical simulations of cloud–corona interactions (Marinacci et al. 2010). A follow-up analysis (Marinacci et al. 2011) indicate that there is a net transfer of momentum from the fountain to the corona until the relative velocity between these two, v_{rel} , reaches a certain threshold v_{thres} . Marinacci et al. (2011) suggested $v_{\text{thres}} \approx 75 \text{ km s}^{-1}$ for initial conditions valid for the Milky Way but pointed out that v_{thres} can vary in the range $45\text{--}105 \text{ km s}^{-1}$ (see also Fraternali 2017). As soon as v_{rel} becomes smaller than this threshold v_{thres} , the net momentum transfer ceases as the condensation of corona recaptures angular momentum lost

by fountain gas. For this reason, we set the azimuthal speed of the corona to be always lower than the local circular speed v_c by v_{thres} , and in this case, $v_c - 75 \text{ km s}^{-1}$. In Section 5.1 we explore models with different value of v_{thres} , corresponding to different rotational speeds for the coronal gas.

In the earlier scenario, the cloud acceleration due to interaction with the corona is defined as

$$\dot{\mathbf{v}} = \begin{cases} -\frac{C\rho_{\text{hot}}\sigma_{\text{cloud}}(v_{\text{rel}}-v_{\text{thres}})}{M_{\text{cloud}}}\mathbf{v}_{\text{rel}} - \alpha\mathbf{v}_{\text{rel}}, & v_{\text{rel}} \geq v_{\text{thres}} \\ -\alpha\mathbf{v}_{\text{rel}}, & v_{\text{rel}} < v_{\text{thres}}, \end{cases} \quad (3)$$

where \mathbf{v}_{rel} is the cloud-corona relative velocity vector, v_{rel} is the modulus of \mathbf{v}_{rel} , M_{cloud} , and σ_{cloud} are the mass and the cross-section of the cloud (defined as πR_{cloud}^2 , with R_{cloud} the radius of the cloud), ρ_{hot} is the density of the corona, C is a dimensionless constant of order unity (in our model $C = 1$) to account for the geometry of the cloud, and α is the condensation rate of the coronal gas onto the cloud, such that the mass of the cloud M_{cloud} grows with time as $\dot{M}_{\text{cloud}} = \alpha M_{\text{cloud}}$. We assume a corona density of 10^{-3} cm^{-3} , a cloud radius of 100 pc and an initial mass of $2 \times 10^4 M_{\odot}$, consistent with typical values of fountain clouds suggested by observations (Hsu et al. 2011).

The first term on the right-hand side of equation (3) represents the drag experienced by the fountain cloud as it moves through the coronal gas: the cloud speed decreases as long as its velocity stays above v_{thres} . The second term is due to the condensation of coronal gas onto the cloud: as the total mass of the cloud increases, conservation of the total momentum implies lower velocity (see FB08). We have also derived the drag time scale $t_{\text{drag}} = 724 \text{ Myr}$ using equation (6) in Fraternali (2017), which is larger than the fountain orbit time ($\sim 100 \text{ Myr}$), we therefore expect that drag only has a minor effect.

In fountain + corona accretion models, we let α be a free parameter with a flat prior in the range $\alpha = 0-6 \text{ Gyr}^{-1}$.

2.4 EPG mass

The normalization of the H I flux presented in the final galactic fountain model sets the total H I EPG mass, which is another free parameter. We use a fiducial EPG mass of $5.9 \times 10^8 M_{\odot}$ from Marasco et al. (2019) as an initial guess, but allow the EPG mass to vary, multiplying the fiducial value by a normalization scaling factor in the range 0.1–10.

3 IMPLEMENTATION OF THE MODEL

In this section, we describe the gravitational potential and the SFR surface-density radial profile for NGC 2403, as they are necessary ingredients to construct our dynamical models. We then describe how we fit the model parameters to the data.

3.1 The gravitational potential

We use the gravitational potential grid derived by FB06 for NGC 2403 without modification. Later we briefly describe how the potential model is built.

The gravitational potential was derived from an axisymmetric mass model, which consists of three components: a stellar disc, a gaseous disc, and an NFW dark matter halo (Navarro, Frenk & White 1997). FB06 performed a mass decomposition of the H I rotation curve of NGC 2403 (Fraternali et al. 2002) using the three components mentioned earlier. The stellar and the gaseous discs' density distributions were given by exponential profiles, along both the radial (R) and the vertical (z) direction. The scale length of the

Table 2. Mass models for NGC 2403.

$(M/L)_*$	R_*	h_*	R_{gas}	h_{gas}	ρ_0, DM	r_s
(1)	[kpc]	[kpc]	[kpc]	[kpc]	$[M_{\odot} \text{ kpc}^{-3}]$	[kpc]
1.70	2.0	0.4	5.7	0.1	3.1×10^7	4.5

Columns: (1) Mass-to-light ratio in the B -band of the stellar disc. (2)–(3): Scale length and scale height of the stellar disc. (4)–(5): Scale length and scale height of the gaseous disc. (6)–(7) Central density and scale radius of the NFW dark matter halo.

stellar (gaseous) disc R_* (R_{gas}) was derived by fitting an exponential profile to the stellar (gaseous) surface brightness radial profile. The scale height of the stellar disc was set to one-fifth of its scale length (see van der Kruit & Freeman 2011 and references therein), and the scale height of the gaseous disc was set to 100 pc (typical of the inner gaseous disc, see Marasco et al. 2017; Bacchini et al. 2019; Mancera Piña et al. 2022). The mass-to-light ratio of the stellar disc was derived via the rotation curve decomposition. The earlier parameters of the mass model are listed in Table 2. Once the parameters of all components are decided, the galactic potential and forces are calculated numerically in the (R, z) cylindrical coordinate system, using a grid with a cell size of 0.1 kpc within $R < 25 \text{ kpc}$ and $z < 5 \text{ kpc}$, and of 0.5 kpc for $25 < R < 100 \text{ kpc}$, and $5 < z < 100 \text{ kpc}$. Potential and forces are determined at any (R, z) via a bilinear interpolation of these grids (see FB06 for details).

3.2 Star-formation-rate surface-density profiles

In this paper, we directly use the SFR surface-density radial profiles from previous observations, as opposed to FB06, which used the Schmidt–Kennicutt law (Kennicutt 1989), and M12, which used another empirical star-formation law (directly derived from 17 galaxies with known gas and SFR surface densities) to estimate the SFR.

The SFR surface-density profile of NGC 2403 is mainly taken from Leroy et al. (2008), which derived the SFR using a combination of far ultraviolet (FUV) and $24 \mu\text{m}$ data, and is then complemented with the SFR surface-density profile from Bigiel et al. (2010), which is derived from FUV data with a lower resolution but larger radial extent compared to Leroy et al. (2008). We refer the readers to Bacchini et al. (2019), Bacchini et al. (2020) for more details about collecting SFR data of NGC 2403. Fig. 1 shows the SFR surface-density data and the interpolated profile (in steps of 0.5 kpc) which we used as an input for our fountain models.

3.3 Separation of the EPG emission

Before modelling the EPG in the NGC 2403 data cube, we first need to isolate its emission from the underlying disc and from external regions (foreground and background emission) that are clearly not associated with the galaxy. For this purpose, we follow the procedure described in Marasco et al. (2019).

The emission from regions external to the galaxy is filtered out by spatially smoothing the data cube by a 2D Gaussian kernel with a full width half maximum (FWHM) of $64''.5 \times 54''.6$, which is five times larger than the spatial resolution of the data, calculating a smoothed rms noise level, and then sigma-clipping at $S/N = 4$. This produces a mask that is applied to the original (not smoothed) data to exclude the regions external to the main galaxy.

In intermediate-inclination galaxies like NGC 2403, the emission from the EPG overlaps spatially with that from the regularly rotating

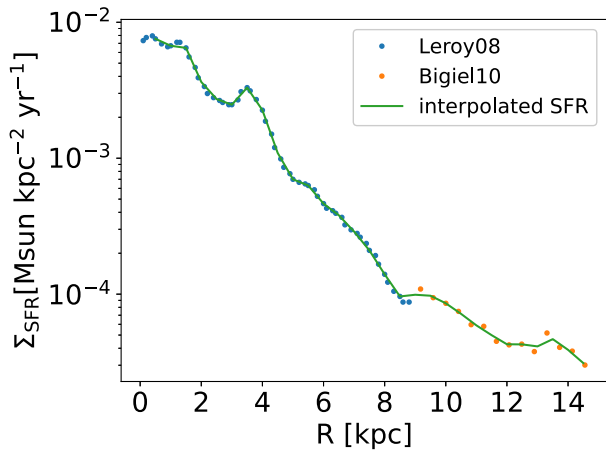


Figure 1. Star-formation rate surface density versus galactocentric distance in NGC 2403. Blue dots represent data from Leroy et al. (2008) while orange points are from Bigiel et al. (2010). The green curve shows the interpolated profiles with steps of 0.5 kpc and is used as an input for our fountain model.

disc but can be (at least in part) separated from the latter in the velocity space, provided that the velocity resolution is sufficient. Here, we employ the disc–EPG separation method introduced by Fraternali et al. (2002), which works as follows. For any given HI velocity profile at a certain location in the sky, the disc component is assumed to be described by a Gaussian profile. The EPG adds a wing to the profile, which is typically due to the lagging of EPG and located toward the systemic-velocity side; although wings on both sides can be seen at some spatial locations across the disc due to other non-circular (mostly vertical) motions (see also Boomsma et al. 2008). Despite the disc and EPG profiles are blended together, it is reasonable to neglect the contribution of the EPG around the peak of each velocity profile since EPG mass is only a small percentage (~ 20 per cent for NGC 2403, Marasco et al. 2019) of the total HI mass. We therefore use the ‘peak’ region to fit the disc emission by performing a Gaussian fit using only the upper 40 per cent (in intensity) of the line profile. This Gaussian profile is considered to be the contribution of emission from the disc component alone. Pixels with disc emission (estimated from the Gaussian profile) larger than N times the rms noise are clipped (see Marasco et al. 2019 and Li et al. 2021 for a more detailed explanation of this methodology). The scaling factor N is decided empirically as a compromise between keeping enough EPG emission for the modelling and alleviating the disc contamination. We set $N = 2$ for NGC 2403.

Some peculiar features in NGC 2403, in particular, a long filament of unknown origin (see also de Blok et al. 2014) have also been manually filtered out (see blank regions in Figs 2 and 3). We discuss this further in Section 5.1.

After passing through the above mask, only EPG emission and noise remain in the data cube. We then implement sigma-clipping at $S/N = 2$ to mask the random noise. For consistency, the same mask has also been applied to the model data cube that we describe later.

3.4 Model construction and evaluation

Our EPG models have three or four free parameters: the characteristic outflow velocity h_v , the ionization fraction f_{ion} , the condensation rate α (for fountain + corona accretion models), and the EPG mass M_{EPG} . We build 3D (4D) grids for pure fountain (fountain + corona accretion) models with h_v varying from 40 to 100 km s^{-1} in steps of 10 km s^{-1} , f_{ion} varying from 0.0 to 1.0 in steps of 0.2, α varying from

0 to 6 Gyr^{-1} in steps of 0.6 Gyr^{-1} , and scaling factor of the initial EPG mass varying from 0.1 to 10 in steps of factor of $10^{0.2}$. The ranges and steps of the free parameters are summarized in Table 3.

The best-fitting parameters are estimated by a Bayesian approach. For each cell in our 3D (4D) parameter grid, we compute the posterior probability of our model. For a chosen parameter vector \mathbf{x} and given our data \mathcal{D} , the posterior probability \mathcal{P} is given by

$$\mathcal{P}(\mathbf{x}|\mathcal{D}) \propto \mathcal{P}(\mathcal{D}|\mathbf{x})\mathcal{P}(\mathbf{x}), \quad (4)$$

where $\mathcal{P}(\mathcal{D}|\mathbf{x})$ is the likelihood function and $\mathcal{P}(\mathbf{x})$ is the prior. The prior for each parameter is uniform within the parameter space (uniform in the logarithmic scale for the normalization parameter). The likelihood function is given by

$$\begin{aligned} \mathcal{P}(\mathcal{D}|\mathbf{x}) &\propto \prod_{n.\text{voxels}} \exp\left(-\frac{|\mathcal{M}(\mathbf{x}) - \mathcal{D}|}{\varepsilon}\right) \\ &= \exp\left(-\sum_{n.\text{voxels}} \frac{|\mathcal{M}(\mathbf{x}) - \mathcal{D}|}{\varepsilon}\right) \\ &= \exp[-\mathcal{R}(\mathbf{x})/\varepsilon], \end{aligned} \quad (5)$$

where \mathcal{M} represents the model data cube built from parameter vector \mathbf{x} , ε is the uncertainty of the data, and \mathcal{R} is the sum of the absolute residuals between the data and the model, which is defined as the sum of absolute difference in each pixel: $\text{Res} = \sum |\text{data} - \text{model}|$. Note that both the model and the data have been masked using the method described in Section 3.3, that is, the voxels where EPG emission is detected at more than 2σ are considered in the determination of the residuals. In equation (5), ε regulates how rapidly the likelihood drops when our model deviates from the data. Assuming ε equal to the rms-noise of the data is a poor choice, which leads to very narrow posterior probability distributions and severely underestimates the uncertainties in our model parameters. This occurs because our model is smooth and axisymmetric, and cannot possibly capture the complexity of the data down to the noise level. Numerical solutions to this problem can be worked out (see Section 2.5 in Marasco et al. 2019), but in this work, we prefer to set ε a posteriori, in a way that the 2σ uncertainty on the derived parameters corresponds to models that look very different from the data by visual inspection. In the end, we assume $\varepsilon = 0.38 \text{ Jy beam}^{-1}$. We marginalize the multidimensional posterior distribution to determine the probability distribution of individual parameters. Best-fitting values are defined as the median of these marginalized posterior distributions, and the uncertainties are taken as half the difference between the 84th and 16th percentiles of the distribution.

4 RESULTS

4.1 Residuals and position-velocity diagrams

In this Section, we show the best-fitting results of the pure fountain and the fountain + corona accretion models. The 2D marginalized posterior probability distributions are shown in Appendix A. The best-fitting values and uncertainties, obtained with the method described in Section 3.4, are listed in Table 4.

The pv slices of the best-fitting models are compared with the data in Figs 2 and 3. In general, both the pure fountain and fountain + corona accretion models recover the EPG emission, but we find that the former reproduces the data poorly for pv slices parallel to the minor axis. Instead, the fountain + corona accretion model performs better in the same locations. This is better shown in Fig. 4, where we compare the two models for a pv slice parallel to the minor axis with

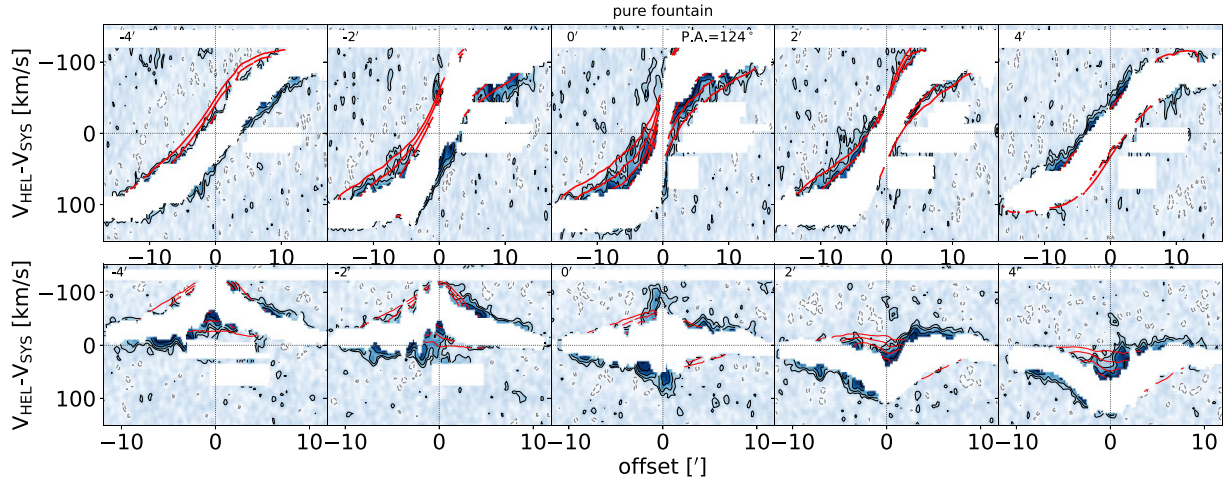


Figure 2. Position–velocity (pv) slices from the data (shown in black contours and blue colour scale) and from the best-fitting pure fountain model (red contours); from outer to inner regions, contour levels are (2, 4, 8, and 16)- σ , respectively, and a negative contour -2σ is shown as the dashed-grey contour. The (irregular) blank region represents the disc mask and the square blank region represents the manual mask that filters out the irregular filament in NGC 2403. Top panels are pv slices parallel to the major axis with offsets $-4'$, $-2'$, $0'$, $2'$, and $4'$. Bottom panels are pv slices parallel to the minor axis with offsets $-4'$, $-2'$, $0'$, $2'$, and $4'$.

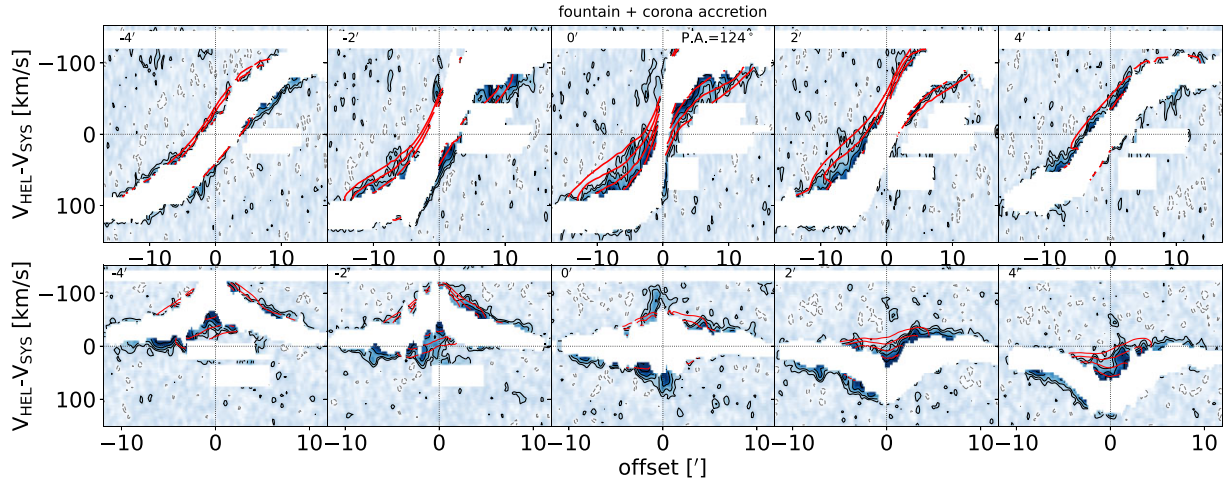


Figure 3. As in Fig. 2, but for the best-fitting fountain + corona accretion model of NGC 2403.

Table 3. Free parameters of our galactic fountain model. The third column lists the range explored in our residual calculations, using a grid size given by the fourth column. ^a a value of 1 corresponds to the EPG mass determined by Marasco et al. (2019) ($5.9 \times 10^8 M_{\odot}$).

Parameter	Description	Range	Step	Units
h_v	Characteristic outflow velocity (equation (1))	[40, 100]	10	km s^{-1}
f_{ion}	Ionization fraction during the ascending part of the orbits (equation (2))	[0, 1.0]	0.2	
α	condensation rate of coronal gas (equation (3))	[0, 6.0]	0.6	Gyr^{-1}
Norm	EPG mass scaling factor ^a	[0.1, 10]	$10^{0.2}$	

an offset $4'$ from the centre. The best-fitting pure fountain model fails to reproduce the emission marked out by the red arrow and predicts extra emission in the blank region marked out by the black arrow. Instead, the best-fitting fountain + corona accretion model generates the same asymmetry shown by the data. Previous studies (Fraternali et al. 2002; Marasco et al. 2019) have shown that this asymmetric feature can be produced by radial inflows. In a fountain model, EPG emission shows outward radial flows, but accretion from low-angular momentum material can invert this trend and produce an inward flow

(especially evident for clouds ejected from the outer regions of the disc; Fraternali 2017), which is required to best reproduce the data.

The above visual comparison prefers the fountain + corona accretion model. This result has been already inferred by FB08, but we now have its statistical confirmation using the likelihood values derived by equation (5). We find $-\ln[\mathcal{P}(\mathcal{D}|\mathbf{x})] = 232.6$ for the best-fitting pure fountain model, while $-\ln[\mathcal{P}(\mathcal{D}|\mathbf{x})] = 224.5$ for the best-fitting fountain + corona accretion model, as shown in Table 4. We use the Bayesian information criterion (BIC; Schwarz

Table 4. The best-fitting values and uncertainties (obtained with the method described in Section 3.4) for our fountain (+ corona accretion) models of the EPG of NGC 2403.

Model	v_{thres} [km s ⁻¹]	h_v [km s ⁻¹]	f_{ion}	α [Gyr ⁻¹]	\dot{m} [M _⊙ yr ⁻¹]	M _{EPG} [10 ⁸ M _⊙]	− ln \mathcal{L}	BIC
(1)	(2)	(3)	(4)	(5)	(6)	(7)	(8)	(9)
Pure fountain	N/A	50 ± 10	0.6 ± 0.2	N/A	N/A	5.9 ^{+1.5} _{−1.2}	232.6	490.6
Fountain + corona accretion	75	50 ± 10	0.4 ± 0.2	2.4 ^{+1.8} _{−0.6}	0.8 ^{+0.4} _{−0.2}	4.7 ^{+1.2} _{−0.9}	224.5	482.9
Fountain + corona accretion	45	50 ± 10	0.4 ^{+0.2} _{−0.4}	4.2 ± 1.2	1.1 ^{+0.3} _{−0.2}	4.7 ^{+1.2} _{−0.9}	223.5	480.9

We focus on the first two models in this Section and further discuss the third model in Section 5.1. (1) Model type. (2) The velocity threshold for fountain + corona accretion models. The net transfer of momentum from the fountain to the corona ceases when the relative velocity between these two decreases below this threshold (see Section 2.3). (3) Characteristic outflow velocity. (4) Ionization fraction of the fountain gas. (5) Condensation rate of the hot gas. (6) Global accretion rate of the condensed hot gas onto the disc. Note that this is not a free parameter but a value derived from the best-fitting model. (7) H I EPG mass. (8) Logarithm of the likelihood values $\mathcal{P}(\mathcal{D}|\mathbf{x})$ of the best-fitting models, calculated in equation (5). (9) The BIC values of the best-fitting models, calculated from equation (6).

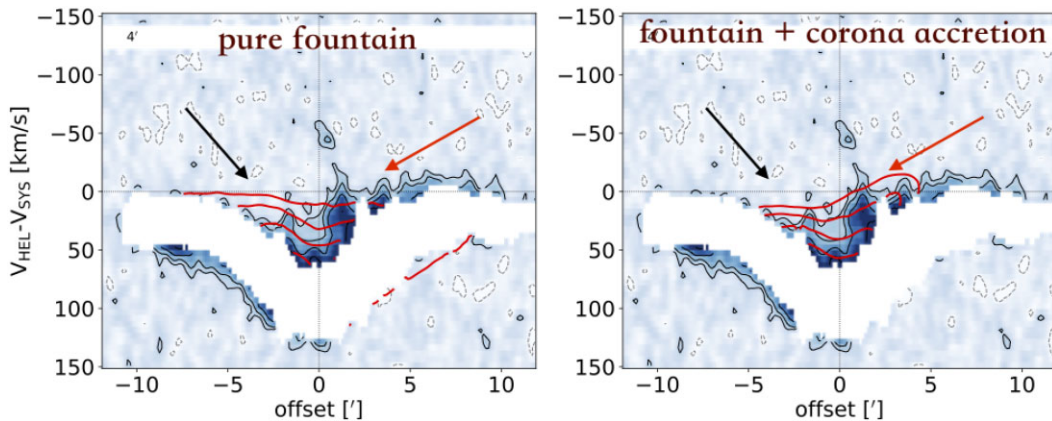


Figure 4. As in Figs 2 and 3, but focusing on the pv slice parallel to the minor axis with offset 4'. Left: best-fitting pure fountain model. Right: best-fitting fountain + corona accretion model. The red arrows mark regions where EPG emission is present in the data and in the fountain + corona accretion model, but not in the pure fountain model. The black arrows mark out the region where the pure fountain model predicts extra emission with respect to the data, while the fountain + corona accretion model correctly predicts a lack of emission.

1978) to infer which of the two different scenarios (pure fountain or fountain + corona accretion) is statistically preferred by the data, given that they make use of a different number of free parameters. The BIC is derived as

$$\text{BIC} = -2 \ln \mathcal{L} + k \ln \mathcal{N}, \quad (6)$$

where \mathcal{L} is the likelihood of the model (equation (5)), k is the number of parameters estimated by the model, and \mathcal{N} is the number of independent data points used in the fit. When comparing similar models with different numbers of free parameters, a model with a lower BIC is to be preferred, as the BIC penalizes extra parameters that do not significantly lower the likelihood. The BIC for the pure fountain model is 490.6 while for the accretion model is 482.9, indicating that the fountain + corona accretion model is statistically preferred by BIC.

The earlier results show that the H I EPG of NGC 2403 is constituted by a combination of material ejected from the disc by stellar feedback and gas cooling from the inner hot CGM and accreting onto the disc. This is also consistent with previous indication from kinematic modelling of the EPG which shows radial and vertical inflow (Marasco et al. 2019). The best-fitting fountain + corona accretion model requires an outflow with a characteristic velocity of $50 \pm 10 \text{ km s}^{-1}$, starting out mostly ionized and becoming neutral when the vertical velocity has been reduced by around 40 per cent. The inferred H I total mass of the EPG ($4.7^{+1.2}_{-0.9} \times 10^8 \text{ M}_{\odot}$) is similar

to that derived in Marasco et al. (2019) ($5.9 \times 10^8 \text{ M}_{\odot}$). The accretion rate given by our best-fitting model ($0.8^{+0.4}_{-0.2} \text{ M}_{\odot} \text{ yr}^{-1}$) is compatible with the star-formation rate of NGC 2403 ($0.6 \text{ M}_{\odot} \text{ yr}^{-1}$; Heald et al. 2012)², indicating that the mechanism of fountain-driven gas accretion can sustain the ongoing star formation in NGC 2403. It is noteworthy that the values of both outflow speed and accretion rate found with our statistical analysis are in agreement with those found by FB08 by trial and error. The present analysis, however, allows us to further our understanding of fountain-driven accretion in NGC 2403.

4.2 Properties of the EPG layer in NGC 2403

This is the first time that a dynamical fountain model including corona condensation has been applied to an external galaxy with a statistical fitting method. The best-fitting fountain + corona accretion model reproduces most of the EPG features in NGC 2403. Assuming our model is reliable and correct (see discussion in Section 5.1), we can therefore extract physical properties of the EPG layer, as well as a predicted gas accretion profile, from the model.

²This estimate has an uncertainty of around ± 0.3 dex or better, based on the algorithm Heald et al. (2012) used to derive the SFR (Kennicutt et al. 2009).

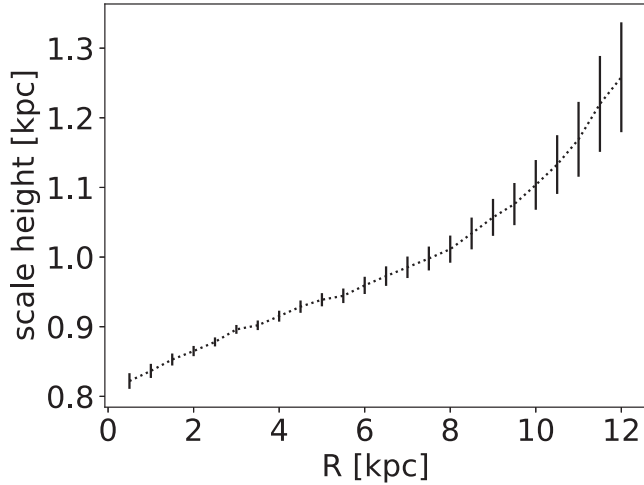


Figure 5. The scale height of the EPG layer predicted by our best-fitting fountain + corona accretion model for NGC 2403.

4.2.1 Thickness of the neutral EPG layer

We determine the thickness of the EPG layer in our best-fitting model by fitting the vertical density profiles at different radii with exponential functions. Fig. 5 shows the scale height of the EPG in our best-fitting fountain + corona accretion model as a function of radius. The scale height is calculated only out to $R = 12.5$ kpc, as fountain clouds beyond this radius are too rare to provide a reliable vertical profile. Overall, the thickness of the gas layer increases slightly with radius, which is what we would expect given that the gravitational potential is shallower in the outer parts of the galaxy (we have assumed that h_v is constant with radius for simplicity, see also Section 5.1). This makes the orbits more extended in the outer region than in the inner region. The flux-weighted average scale height of our EPG model is 0.93 ± 0.003 kpc, compatible with the scale height derived in the kinematic model in Marasco et al. (2019). Thus, the EPG layer of NGC 2403 is significantly thicker than its HI disc, which has scale height comprised between 100 and 600 pc (Mancera Piña et al. 2022).

4.2.2 EPG rotational lag

Fig. 6 shows the rotation curves of the EPG layer at different heights above the disc. These curves are derived from our best-fitting fountain + corona accretion model by taking the flux-weighted mean value of the azimuthal velocities of the particles in a given bin of radius and height. We find that the rotation velocity of the EPG decreases with height. At $R = 5.5$ kpc (the half-mass radius of the EPG in NGC 2403), the velocity gradient is around -10.0 ± 2.7 km s⁻¹ kpc⁻¹. This gradient is consistent with the velocity gradient of -11.7 ± 0.5 km s⁻¹ kpc⁻¹ inferred by Marasco et al. (2019), who modelled the EPG of NGC 2403 with simplified geometric and kinematic assumptions, and therefore intrinsically differs from our dynamical model. Our results are also comparable with the velocity gradient -15 ± 0.5 km s⁻¹ kpc⁻¹ directly measured in the edge-on galaxy NGC 891.

4.3 Gas flows and accretion in NGC 2403

Fig. 7 shows the inflow and outflow rates as a function of radius predicted by our best-fitting fountain + corona accretion model. The shape of the outflow rate profile strictly follows that of the SFR profile

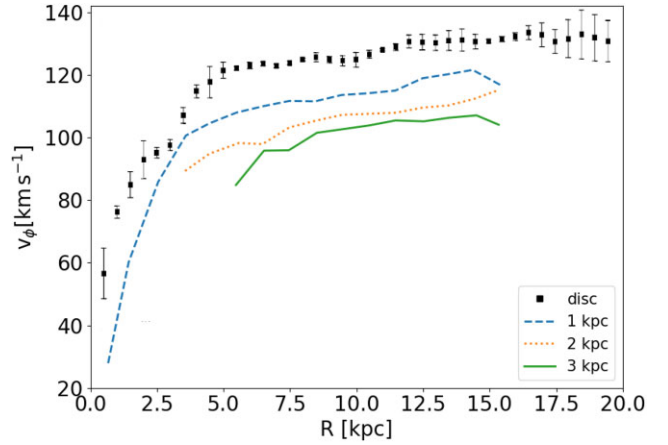


Figure 6. Rotational velocities for the EPG layer at different heights from the plane (solid/dashed/dotted lines), compared to the disc rotation curve (black squares with error bars) given by Fraternali et al. (2002). Velocities are derived from our best-fitting fountain + corona accretion model by taking the flux-weighted average of azimuthal velocity v_ϕ at given (R, z) locations.

shown in Fig. 1. This is true by construction, as explained in Section 2. The mass loading factor (defined as the ratio of the mass outflow rate to the SFR and therefore is proportional to the normalization factor free parameter in our model) is however a prediction of our model, and we find a value of around 9.5. The inflow rate at a given radius is given by the combination of fountain clouds and accreted coronal particles that fall onto the disc per unit time and area. Since fountain clouds do not fall back onto the disc at the same radius as they are ejected and collect additional gas condensed from the corona as they fall, the inflow rates do not precisely follow the outflow-rate trend but show a somewhat smoother distribution.

We also present the net flow rate (where inflow is defined as positive value) as a function of radius in Fig. 7 top panel. The first evident feature is that the net flow is much lower than both outflow and inflow across the disc, except for the very outer parts. Also, except for some fluctuation in the innermost region (within $R = 4$ kpc), the overall tendency is net inflow in the inner region ($R < 10.5$ kpc, the vertical-dashed line in Fig. 7 top panel) and net outflow in the outer region. The net inflow is mostly due to condensation of the hot corona, while the net outflow in the outer region can be explained by the fact that the interaction between fountain gas and the corona results in inward orbits for the former: cloud particles are more likely to fall back to the plane at a radius smaller than their ejected radius (see fig. 8 in Fraternali 2017).

As we discussed in Section 1, accretion of the CGM onto the disc is crucial for feeding star formation and is also a key process in the evolution of a galaxy. The details of this process are however not well understood. Now with our best-fitting fountain + corona accretion model, we can predict the accretion rate as a function of radius, shown in the bottom panel of Fig. 7. Despite star formation being the origin of the fountain cycle, the fountain-driven accretion rate does not follow the profile of the SFR surface density (shown in Fig. 1) and in particular, it is more skewed towards larger radii compared with the SFR surface-density profile. This is due to a number of effects, the most important of which is a radially increasing orbital time, which is in turn a consequence of a varying gravitational potential with radius, as also discussed in Section 4.2.1. A longer orbital time causes an increase in the total condensation along a given orbit, even with a fixed accretion efficiency per unit time (i.e. α), as assumed in our model. The accretion profile has a well-defined peak at intermediate

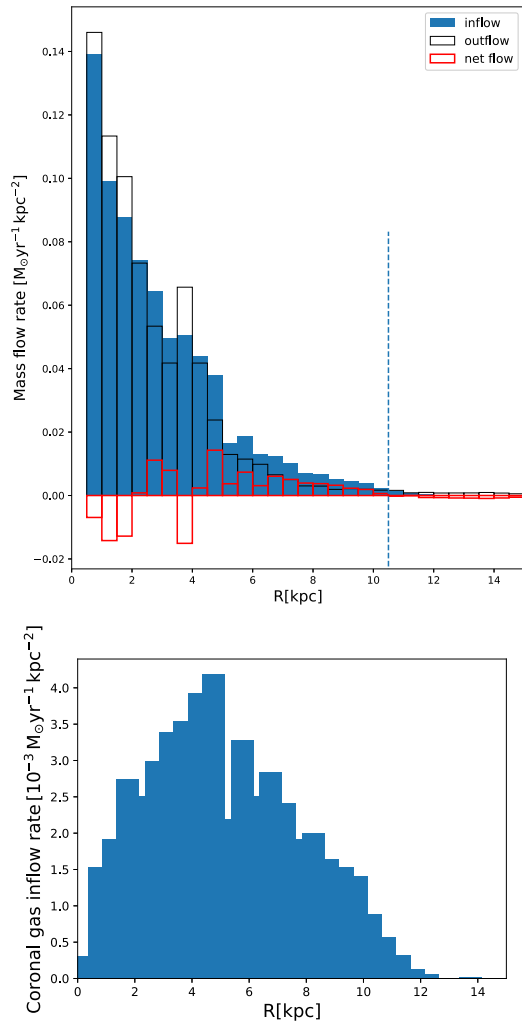


Figure 7. Inflow and outflow rate surface density as a function of radius predicted by our best-fitting fountain + corona accretion model of NGC 2403. Top panel: inflow rates (blue bars), outflow rates (black bars), and net flow rates (red bars: inflow–outflow; positive values indicate net inflow). The vertical-dashed line at 10.5 kpc marks the boundary where the net flow changes from inflow to outflow. Bottom panel: inflow rate surface density contributed by corona accretion, the integration of which gives us the global accretion rate of $0.8 M_{\odot} \text{ yr}^{-1}$.

radii and its exact position is determined by an interplay between a radially declining SFR surface density and a radially increasing duration of the orbits (see also M12 for the Milky Way).

The gas accretion rate that comes from corona condensation is at every radius a minor fraction of the overall gas inflow (~ 10 per cent; see Fig. 7). Compared to the total accretion rate of $0.8 M_{\odot} \text{ yr}^{-1}$, the total inflow and outflow rates are $6.48 M_{\odot} \text{ yr}^{-1}$ and $5.69 M_{\odot} \text{ yr}^{-1}$, respectively. Most of the gas inflow occurs as a consequence of the return to the disc of the gas ejected by the fountain. However, the fountain cycle by itself does not add any new gas to the disc and would not help to sustain the star formation. Instead, our model predicts that the fountain flow ‘captures’ new gas from the corona, that is, then added everywhere across the disc to sustain the local star formation. Remarkably, the accretion rate that is needed to reproduce the seemingly independent kinematics of the EPG in NGC 2403 turns out to be very similar to the one needed to sustain its star formation.

Overall, the accretion rate peaks at around 4.5 kpc and the cumulative accretion rate reaches 50 per cent of the total accretion rate at 6.25 kpc. As we mentioned, this distribution is shifted outwards with respect to the SFR surface-density distribution, which peaks in the centre of NGC 2403 and reaches 50 per cent of the total SFR at 3.3 kpc. The relevance of this difference is further discussed in Section 5.2.

5 DISCUSSION

5.1 Reliability of the fountain + corona accretion model

In this paper, we have investigated gas accretion as the potential mechanism to maintain star formation in NGC 2403 and found a remarkable consistency between the accretion rate predicted by our model and the SFR. However, accretion is not the only fuelling mechanism. Several studies have pointed out the importance of stellar mass-loss in extending gas consumption time scales (e.g. Sandage 1986; Kennicutt, Tamblyn & Congdon 1994) and sustaining star formation (e.g. Schaye et al. 2010; Leitner & Kravtsov 2011). In particular, Leitner & Kravtsov (2011, hereafter LK11) has estimated the current stellar mass-loss rate of NGC 2403 to be $0.5 - 0.79 M_{\odot} \text{ yr}^{-1}$ (depending on the underlying initial mass function), which seems to eliminate the need of gas accretion. However, this mass-loss rate was calculated in LK11 assuming a SFR of $1.3 M_{\odot} \text{ yr}^{-1}$, implying that the stellar mass-loss can sustain at most 60 per cent of the SFR of NGC2403, while at least 40 per cent must be due to gas accretion. Note that the estimation of the mass-loss rate is dependent on the SFR: a lower SFR would result in a lower mass-loss rate (although not necessarily in proportion). Overall, we conclude that gas accretion is still necessary to sustain the SFR in NGC 2403 within the circumstances explored by the LK11 model.

In Section 4 we explored four free parameters that are crucial for our EPG dynamical model. However, construction of the model also involves other parameters and ingredients for which we make specific choices. Later we discuss the limitations and reliability of our model.

The gravitational potential of NGC 2403 used in this paper is generated from a mass model consisting of three components: a stellar disc, a gaseous disc, and a dark matter halo. The parameters of the mass model are inferred via rotation curve decomposition (FB06). Given that the circular velocity generated from the mass model is consistent with the rotation curve of NGC 2403 (see FB06), we conclude that the gravitational potential is robust. The only uncertainty is related to the fraction of the stellar disc contribution to the potential, parametrized by the mass-to-light ratio. The gravitational potential used in the earlier analysis was based on the maximum-disc model shown in Table 2. It is however noteworthy that the minimum disc potential in FB06 is in fair agreement with those derived more recently with more sophisticated methods (Mancera Piña et al. 2022). FB06 have experimented with both maximum disc and minimum disc potentials and showed that the dynamics of the EPG does not change significantly.

An assumption of our model is the existence of a uniform characteristic outflow velocity at all radii, whereas the varying stellar feedback activities might lead to outflow velocities changing with radius. Allowing spatial variations in the characteristic outflow velocity is a potential improvement for this kind of study. This has been briefly explored in FB06 to generate specific features in N2403 (e.g. the filament shown in channel 104.1 km s^{-1} and channel 135.0 km s^{-1} of fig. 14 in FB06) that are otherwise not reproduced. However, exploring the variation of h_v with radius would introduce at

least one extra free parameter, which would significantly complicate our exploration of the parameter space. Overall, the global kinematics of the EPG in NGC 2403 appears to be well reproduced by a constant characteristic outflow speed across the disc.

In the fountain + corona accretion scenario, the acceleration of fountain gas is directly dictated, besides by gravity, by the velocity difference between the fountain and the corona. In our model, we assume a relative azimuthal velocity of 75 km s^{-1} between the fountain gas and the corona, based on hydrodynamical simulations (Marinacci et al. 2011). Such a high relative velocity would imply a rather slowly rotating corona in NGC 2403, given the disc rotation of around 130 km s^{-1} (FB06). We have therefore tested models with a lower relative velocity of 45 km s^{-1} that result in nearly identical best-fitting parameters as in Section 4.1 except for a higher condensation rate ($4.2 \pm 1.2 \text{ Gyr}^{-1}$), which corresponds to a global accretion rate of $1.1^{+0.3}_{-0.2} M_{\odot} \text{ yr}^{-1}$ (the best-fitting results are listed in Table 4). This higher rate is not surprising. In our model, as a consequence of condensation, the coronal gas joins the cold/warm phase of the fountain gas such that the velocity of a single cloud evolves as a combination (mass-weighted average) of the kinematics of the two components (cloud and condensed material). If the velocity difference between these two components is reduced, one needs a larger accretion rate (more condensed material) to produce the same effect in the combined kinematics. It is noteworthy that EPG models built with a lower relative velocity have lower velocity gradients than what we show in Fig. 6. However, the difference ($1.0 \text{ km s}^{-1} \text{ kpc}^{-1}$) is negligible, given that the uncertainty for our measurement is $2.7 \text{ km s}^{-1} \text{ kpc}^{-1}$.

The separation of EPG emission from the data cube is an important ingredient of our method. The reliability of our strategy for masking the disc emission has been verified in several previous studies (e.g. Fraternali et al. 2002; Marasco et al. 2019; Li et al. 2021). We have tested the robustness of our results by fitting the data without masking the peculiar H I filament of NGC 2403, finding the same normalization factor as shown in Table 4, but an h_v of 60 km s^{-1} , an f_{ion} of 0, a condensation rate of 4.8 Gyr^{-1} , leading to an accretion rate of $1.28 M_{\odot} \text{ yr}^{-1}$ (all parameters are compatible with those of our fiducial model within the errors.). Thus models with slightly higher outflow velocities and condensation rates are preferred to account for the filament in NGC 2403, but the overall validity of our results is not particularly affected by our masking.

In conclusion, the construction of our dynamical model is robust. The variation of certain ingredients leads to small changes in the model best-fitting parameters but does not alter our main conclusion: the EPG of NGC 2403 is produced by a combination of galactic fountain clouds and gas accretion from the condensation of the hot CGM at a rate compatible with the SFR of the galaxy.

5.2 Can the fountain + corona accretion sustain the inside-out growth of the disc?

Since accretion is a key source to fuel further star formation, the outward shift of the accretion (compared to the SFR) shown in Section 4.3 suggests a potential inside-out redistribution of gas and star-formation activities in the future, which has been predicted by cosmological simulations (e.g. Grand et al. 2017) and supported by many observations (e.g. Wang et al. 2011; van der Wel et al. 2014; Pezzulli et al. 2015). Pezzulli et al. (2015) also provided measurements of the specific radial growth rate, $v_R \equiv (1/R_*) \times dR_*/dt$, where R_* is the scale length of the stellar disc, for a sample of galaxies including NGC 2403. Furthermore, a cosmological/zoom-in

simulation (Grand et al. 2019) also found that fountain clouds can acquire angular momentum via interaction with the CGM.

To verify whether the gas accretion due to a galactic fountain can be deemed responsible for this growth, we calculated the variation in time of the specific angular momentum dj/dt of the stellar disc (a direct tracer of disc growth; Mo, Mao & White 1998; Posti et al. 2019) due to accretion, under the simplifying assumption that the next generation of stars will be formed out of the newly accreted gas. This gives

$$\begin{aligned} \frac{dj}{dt} &= \frac{d(J/M)}{dt} \\ &= \frac{1}{M} \frac{dJ}{dt} - \frac{J}{M^2} \frac{dM}{dt}, \end{aligned} \quad (7)$$

where J and M ($7.2 \times 10^9 M_{\odot}$) are the angular momentum and mass of the stellar disc. We estimate J as $J = 2MV_{\text{flat}}R_*$ (Romanowsky & Fall 2012), where V_{flat} is the rotational velocity of the flat part of the rotation curve (130 km s^{-1}) and $R_* = 2.0 \text{ kpc}$ (values from Fraternali et al. 2002). The time derivative of the angular momentum dJ/dt is given by

$$\begin{aligned} \frac{dJ}{dt} &= \frac{dJ_{\text{in}}}{dt} - \frac{dJ_{\text{out}}}{dt} \\ &= 2\pi \int_0^R R'^2 \mathcal{F}_{\text{in}}(R') \overline{V_{\text{in}}(R')} dR' \\ &\quad - 2\pi \int_0^R R'^2 \mathcal{F}_{\text{out}}(R') \overline{V_{\text{out}}(R')} dR', \end{aligned} \quad (8)$$

where \mathcal{F}_{in} (\mathcal{F}_{out}) is the inflow (outflow) surface-density rate given in Section 4.3, $\overline{V_{\text{in}}(R')}$ ($\overline{V_{\text{out}}(R')}$) is the average rotational velocity of all cloud particles falling onto (ejected from) the disc at radius R' , obtained from our model by tracking the outflow and inflow radius and velocity of all fountain clouds. The time derivative of the mass, dM/dt , is by definition the accretion rate of new gas given by the model.

Implementing the earlier equation to our best-fitting model, we have $dj/dt = -2.6 \times 10^{-8} \text{ km s}^{-1} \text{ kpc yr}^{-1}$. This would indicate that the gas accreted through the fountain cannot be solely responsible for the observed inside-out growth of the disc. Part of this growth should then be ascribed to gas that is already present in the disc. This is a viable option, as the gas in the disc is known to be located, on average, at larger radii compared to the stellar component (e.g. Fraternali et al. 2002). This solution is, however, only partly satisfactory, as the gas reservoir at these large radii would, without replacement, be consumed on a relatively short time scale (a few Gyr; see e.g. Fraternali & Tomassetti 2012), implying that the growth of the disc would not be sustainable in the long term.

With these considerations in mind, we stress that our calculation of dj/dt , presented earlier, very much depends on the value that we are assuming for the rotational speed of the corona, which is, as we discussed earlier, very uncertain. Interestingly, when assuming the rotational lag between the fountain and the hot gas is 45 km s^{-1} (the third model in Table 4), we have $dj/dt = 1.5 \times 10^{-8} \text{ km s}^{-1} \text{ kpc yr}^{-1}$, which indicates an inside-out growth. Combining the current value of the specific angular momentum j and its derivative dj/dt , we can easily derive the specific angular momentum growth rate, which we define (following Pezzulli et al. 2015) as $v_j \equiv (1/j) \times dj/dt$. We find a value of $v_j = 2.88 \times 10^{-2} \text{ Gyr}^{-1}$, in excellent agreement with the specific radial growth rate $v_R = (2.93 \pm 0.16) \times 10^{-2} \text{ Gyr}^{-1}$ measured by Pezzulli et al. (2015) for NGC 2403. The two quantities v_j and v_R are comparable and are in fact expected to be equal, as long as the rotation curve of the galaxy can be considered approximately

stationary with time.³ We have therefore found that our model with a reduced rotational lag is in remarkable quantitative agreement with the galactic fountain being the main source of the observed inside-out growth in NGC 2403.

It is important to note that in the absence of triggered condensation, a galactic corona will be expected to cool in the very inner parts, where its density tends to be higher, thus producing the accretion of low angular momentum gas that then would need to be expelled via strong feedback (e.g. Brook et al. 2012). Instead, when the cooling is triggered by the fountain, the location of the bulk of the gas accretion is naturally shifted to outer radii for the reasons described in Section 4.3. This phenomenon had been indicated as plausibly compatible with the inside-out growth of discs (Pezzulli & Fraternali 2016), but this is the first time that quantitative evidence is provided.

6 CONCLUSION

In this work, we have modelled the distribution and kinematics of the neutral EPG in the late-type nearby galaxy NGC 2403 using a dynamical model of galactic fountain. In this model, stellar feedback activities continuously eject gas from the galaxy disc, which travels through the halo and falls back to the disc. This gas cycle brings metal-rich and cold/warm gas to mix and interact with the hot corona, significantly reducing its cooling time, and leading to condensation and accretion of some coronal gas onto the disc. Due to angular momentum exchange between the fountain clouds and the corona, this interaction is expected to leave a signature in the kinematics of the H I gas at the disc–halo interface. The application of our models to the data leverage this signature to infer, along with other parameters, the efficiency of the condensation process and the accretion rate of coronal gas onto the disc.

While these models have been applied extensively to the EPG of the Milky Way (M12; Marasco et al. 2013; Fraternali et al. 2013, 2015), so far applications to external galaxies were limited to the preliminary studies of FB06 and FB08, which did not include a rotating corona nor a statistically meaningful exploration of the parameter space. This study presents the first detailed application of the current fountain accretion framework to an external galaxy. Our results are summarized as follows:

(i) the galactic fountain framework can reproduce most of the neutral EPG features in NGC 2403. A model where the fountain clouds interact with the hot corona is statistically preferred compared to a pure fountain model without interaction with the hot CGM;

(ii) the best-fitting model requires a fountain with a characteristic outflow velocity of $50 \pm 10 \text{ km s}^{-1}$, with the gas being ionized for some time after ejection and then recombining. Recombination appears to occur on average when its vertical velocity has been reduced by about 40 per cent;

(iii) the H I EPG in NGC 2403 inferred from the best-fitting model has a total EPG mass of $4.7_{-0.9}^{+1.2} \times 10^8 M_{\odot}$, with an average scale height of $0.93 \pm 0.003 \text{ kpc}$ and a vertical gradient in rotational velocity of $-10.0 \pm 2.7 \text{ km s}^{-1} \text{ kpc}^{-1}$. Our values are compatible with a previous estimate of Marasco et al. (2019), which was derived with simpler phenomenological approaches;

(iv) our model predicts a condensation rate of 2.4 Gyr^{-1} (4.2 Gyr^{-1}) for the hot CGM, leading to a total accretion rate of $0.8 M_{\odot} \text{ yr}^{-1}$ ($1.1 M_{\odot} \text{ yr}^{-1}$) when assuming the rotational lag between

the fountain and the hot gas is 75 km s^{-1} (45 km s^{-1}), similar to the star-formation rate $0.6 M_{\odot} \text{ yr}^{-1}$ of NGC 2403, suggesting corona accretion as a viable mechanism to maintain the star-formation rate in this galaxy; and

(v) the accretion rate surface-density profile predicted by our model is radially more extended than the SFR surface density. We have also shown that, if the rotation velocity of the corona is larger than a certain threshold, the specific angular momentum growth rate predicted by our model is in excellent agreement with the observed inside-out growth rate in NGC 2403. The fountain-driven accretion process can therefore be responsible for the inside-out growth of its stellar disc.

ACKNOWLEDGEMENTS

The authors would like to thank an anonymous referee for helpful comments and Cecilia Bacchini for collecting and providing the H I, H₂, and SFR data of NGC 2403. AL was supported by the Netherlands Research School for Astronomy (Nederlandse Onderzoekschool voor Astronomie, NOVA), Network 1, Project 10.1.5.9 WEAVE. GP acknowledges support from the Netherlands Research School for Astronomy (Nederlandse Onderzoekschool voor Astronomie, NOVA) through project 10.1.5.18.

DATA AVAILABILITY

The data underlying this article were obtained by Fraternali et al. (2002) with the CS configuration of the VLA and were later included in the HALOGAS survey, which is available at <https://www.astron.nl/halogas>.

REFERENCES

- Afruni A., Fraternali F., Pezzulli G., 2021, *MNRAS*, 501, 5575
 Anderson M. E., Bregman J. N., 2011, *ApJ*, 737, L22
 Anderson M. E., Churazov E., Bregman J. N., 2016, *MNRAS*, 455, 227
 Armillotta L., Fraternali F., Marinacci F., 2016, *MNRAS*, 462, 4157
 Aumer M., Binney J. J., 2009, *MNRAS*, 397, 1286
 Bacchini C., Fraternali F., Iorio G., Pezzulli G., 2019, *A&A*, 622, 64
 Bacchini C., Fraternali F., Pezzulli G., Marasco A., 2020, *A&A*, 644, 125
 Barbieri C. V. F., Oosterloo T., Bertin G., Boomsma R., Sancisi R., 2005, *A&A*, 439, 947
 Bigiel F., Leroy A., Walter F., Blitz L., Brinks E., de Blok W. J. G., Madore B., 2010, *AJ*, 140, 1194
 Binney J., Nipoti C., Fraternali F., 2009, *MNRAS*, 397, 1804
 Boomsma R., Oosterloo T. A., Fraternali F., van der Hulst J. M., Sancisi R., 2008, *A&A*, 490, 555
 Bregman J. N., 1980, *ApJ*, 236, L577
 Brook C. B., Stinson G., Gibson B. K., Roškar R., Wadsley J., Quinn T., 2012, *MNRAS*, 419, 771
 Ciotti L., Ostriker J. P., 2012, in Kim D.-W., Pellegrini S., eds, *Astrophysics and Space Science Library* Vol. 378, *Astrophysics and Space Science Library*. p. 83
 Crain R. A., Eke V. R., Frenk C. S., Jenkins A., McCarthy I. G., Navarro J. F., Pearce F. R., 2007, *MNRAS*, 377, 41
 de Blok W. J. G., et al., 2014, *A&A*, 569, 68
 Dettmar R. J., 1990, *A&A*, 232, L15
 Di Teodoro E. M., Fraternali F., 2014, *A&A*, 567, 68
 Di Teodoro E. M., Peek J. E. G., 2021, *ApJ*, 923, L220
 El-Badry K., et al., 2018, *MNRAS*, 473, 1930
 Faerman Y., Sternberg A., McKee C. F., 2020, *ApJ*, 893, L82
 Fraternali F., 2017, in Fox A., Davé R., eds, *ASSL*, Vol. 430, *Gas Accretion onto Galaxies*. Springer International Publishing AG, p. 323
 Fraternali F., Binney J. J., 2006, *MNRAS*, 366, 449

³This is immediately seen by taking the time derivative of the equation $j = 2V_{\text{flat}}R_*$.

- Fraternali F., Binney J. J., 2008, *MNRAS*, 386, 935
- Fraternali F., Tomassetti M., 2012, *MNRAS*, 426, 2166
- Fraternali F., van Moorsel G., Sancisi R., Oosterloo T., 2002, *AJ*, 123, 3124
- Fraternali F., Marasco A., Marinacci F., Binney J., 2013, *ApJ*, 764, L21
- Fraternali F., Marasco A., Armillotta L., Marinacci F., 2015, *MNRAS*, 447, 70
- French D. M., et al., 2021, *ApJ*, 923, L50
- Fukugita M., Peebles P. J. E., 2006, *ApJ*, 639, L590
- Gatto A., Fraternali F., Read J. I., Marinacci F., Lux H., Walch S., 2013, *MNRAS*, 433, 2749
- Grand R. J. J., et al., 2017, *MNRAS*, 467, 179
- Grand R. J. J., et al., 2019, *MNRAS*, 490, 4786
- Gronke M., Oh S. P., 2018, *MNRAS*, 480, 111
- Heald G., et al., 2011, *A&A*, 526, 118
- Heald G., et al., 2012, The Westerbork Hydrogen Accretion in Local GALaxieS (HALOGAS) survey (Corrigendum). I. Survey description and pilot observations, *Astronomy & Astrophysics*, Vol. 544, id.C1. p. C1
- Heald G. H., Rand R. J., Benjamin R. A., Bershadsky M. A., 2006, *ApJ*, 647, 1018
- Heckman T., Borthakur S., Wild V., Schiminovich D., Bordoloi R., 2017, *ApJ*, 846, L151
- Hess K. M., Pisano D. J., Wilcots E. M., Chengalur J. N., 2009, *ApJ*, 699, L76
- Hodges-Kluck E. J., Miller M. J., Bregman J. N., 2016, *ApJ*, 822, L21
- Hopkins A. M., McClure-Griffiths N. M., Gaensler B. M., 2008, *ApJ*, 682, L13
- Hsu W. H., Putman M. E., Heitsch F., Stanimirović S., Peek J. E. G., Clark S. E., 2011, *AJ*, 141, 57
- Iorio G., Fraternali F., Nipoti C., Di Teodoro E., Read J. I., Battaglia G., 2017, *MNRAS*, 466, 4159
- Joung M. R., Bryan G. L., Putman M. E., 2012, *ApJ*, 745, L148
- Kamphuis P., Peletier R. F., Dettmar R. J., van der Hulst J. M., van der Kruit P. C., Allen R. J., 2007, *A&A*, 468, 951
- Keller B. W., Wadsley J., Benincasa S. M., Couchman H. M. P., 2014, *MNRAS*, 442, 3013
- Kennicutt R. C. J., et al., 2009, *ApJ*, 703, L1672
- Kennicutt R. C. J., 1989, *ApJ*, 344, L685
- Kennicutt R. C. J., Tamblyn P., Congdon C. E., 1994, *ApJ*, 435, L22
- Kereš D., Katz N., Weinberg D. H., Davé R., 2005, *MNRAS*, 363, 2
- Kereš D., Katz N., Fardal M., Davé R., Weinberg D. H., 2009, *MNRAS*, 395, 160
- Kim C.-G., Ostriker E. C., 2018, *ApJ*, 853, L173
- Kooij R., Grønnow A., Fraternali F., 2021, *MNRAS*, 502, 1263
- Lagos C. d. P., Theuns T., Stevens A. R. H., Cortese L., Padilla N. D., Davis T. A., Contreras S., Croton D., 2017, *MNRAS*, 464, 3850
- Lehner N., Howk J. C., Thom C., Fox A. J., Tumlinson J., Tripp T. M., Meiring J. D., 2012, *MNRAS*, 424, 2896
- Lehner N., Howk J. C., Marasco A., Fraternali F., 2022, *MNRAS*, 513, 3228
- Leitner S. N., Kravtsov A. V., 2011, *ApJ*, 734, 48
- Leroy A. K., Walter F., Brinks E., Bigiel F., de Blok W. J. G., Madore B., Thornley M. D., 2008, *AJ*, 136, 2782
- Levy R. C., et al., 2019, *ApJ*, 882, L84
- Li A., Marasco A., Fraternali F., Trager S., Verheijen M. A. W., 2021, *MNRAS*, 504, 3013
- Li J.-T., Bregman J. N., Wang Q. D., Crain R. A., Anderson M. E., 2018, *ApJ*, 855, L24
- Mac Low M.-M., McCray R., 1988, *ApJ*, 324, L776
- Mancera Piña P. E., Posti L., Fraternali F., Adams E. A. K., Oosterloo T., 2021, *A&A*, 647, 76
- Mancera Piña P. E., Fraternali F., Oosterloo T., Adams E. A. K., di Teodoro E., Bacchini C., Iorio G., 2022, *MNRAS*, 514, 3329
- Marasco A., et al., 2019, *A&A*, 631, 50
- Marasco A., Fraternali F., 2011, *A&A*, 525, 134
- Marasco A., Fraternali F., Binney J. J., 2012, *MNRAS*, 419, 1107
- Marasco A., Marinacci F., Fraternali F., 2013, *MNRAS*, 433, 1634
- Marasco A., Fraternali F., van der Hulst J. M., Oosterloo T., 2017, *A&A*, 607, 106
- Marasco A., Fraternali F., Lehner N., Howk J. C., 2022, *MNRAS*, 515, 4176
- Marinacci F., Binney J., Fraternali F., Nipoti C., Ciotti L., Londrillo P., 2010, *MNRAS*, 404, 1464
- Marinacci F., Fraternali F., Nipoti C., Binney J., Ciotti L., Londrillo P., 2011, *MNRAS*, 415, 1534
- Mo H. J., Mao S., White S. D. M., 1998, *MNRAS*, 295, 319
- Navarro J. F., Frenk C. S., White S. D. M., 1997, *ApJ*, 490, L493
- Nelson D., Vogelsberger M., Genel S., Sijacki D., Kereš D., Springel V., Hernquist L., 2013, *MNRAS*, 429, 3353
- Nipoti C., 2010, *MNRAS*, 406, 247
- Oosterloo T., Fraternali F., Sancisi R., 2007, *AJ*, 134, 1019
- Pezzulli G., Fraternali F., 2016, *MNRAS*, 455, 2308
- Pezzulli G., Fraternali F., Boissier S., Muñoz-Mateos J. C., 2015, *MNRAS*, 451, 2324
- Pezzulli G., Fraternali F., Binney J., 2017, *MNRAS*, 467, 311
- Pointon S. K., Kacprzak G. G., Nielsen N. M., Muzahid S., Murphy M. T., Churchill C. W., Charlton J. C., 2019, *ApJ*, 883, L78
- Posti L., Marasco A., Fraternali F., Famaey B., 2019, *A&A*, 629, 59
- Putman M. E., Zheng Y., Price-Whelan A. M., Grcevich J., Johnson A. C., Tollerud E., Peek J. E. G., 2021, *ApJ*, 913, L53
- Romanowsky A. J., Fall S. M., 2012, *ApJS*, 203, 17
- Rubin K. H. R., Prochaska J. X., Koo D. C., Phillips A. C., Weiner B. J., 2010, *ApJ*, 712, L574
- Rubin K. H. R., Diamond-Stanic A. M., Coil A. L., Crighton N. H. M., Moustakas J., 2018, *ApJ*, 853, L95
- Sancisi R., Fraternali F., Oosterloo T., van der Hulst T., 2008, *A&A Rev.*, 15, 189
- Sandage A., 1986, *A&A*, 161, 89
- Schaye J., et al., 2010, *MNRAS*, 402, 1536
- Schroetter I., et al., 2019, *MNRAS*, 490, 4368
- Schwarz G., 1978, *Annals of Statistics*, 6, 461
- Shapiro P. R., Field G. B., 1976, *ApJ*, 205, L762
- Stinson G. S., Brook C., Macciò A. V., Wadsley J., Quinn T. R., Couchman H. M. P., 2013, *MNRAS*, 428, 129
- Tacconi L. J., et al., 2018, *ApJ*, 853, L179
- Trapp C. W., et al., 2022, *MNRAS*, 509, 4149
- Tumlinson J., et al., 2011, *Science*, 334, 948
- van der Kruit P. C., Freeman K. C., 2011, *ARA&A*, 49, 301
- van der Wel A., et al., 2014, *ApJ*, 788, L28
- Vijayan A., Kim C.-G., Armillotta L., Ostriker E. C., Li M., 2020, *ApJ*, 894, L12
- Voit G. M., Bryan G. L., O'Shea B. W., Donahue M., 2015, *ApJ*, 808, L30
- Wakker B. P., 2001, *ApJS*, 136, 463
- Walker S. A., Bagchi J., Fabian A. C., 2015, *MNRAS*, 449, 3527
- Wang J., et al., 2011, *MNRAS*, 412, 1081
- White S. D. M., Frenk C. S., 1991, *ApJ*, 379, L52
- Zahedy F. S., Chen H.-W., Johnson S. D., Pierce R. M., Rauch M., Huang Y.-H., Weiner B. J., Gauthier J.-R., 2019, *MNRAS*, 484, 2257
- Zschaechner L. K., Rand R. J., Heald G. H., Gentile G., Kamphuis P., 2011, *ApJ*, 740, L35

APPENDIX A: 2D MARGINALIZED POSTERIOR PROBABILITY DISTRIBUTION

2D marginalized posterior probability distribution maps and contours of the 3D (4D) grids of free parameters (summarized in Table 3) for pure fountain (fountain + corona accretion) models, shown in Figs A1 and A2, respectively.

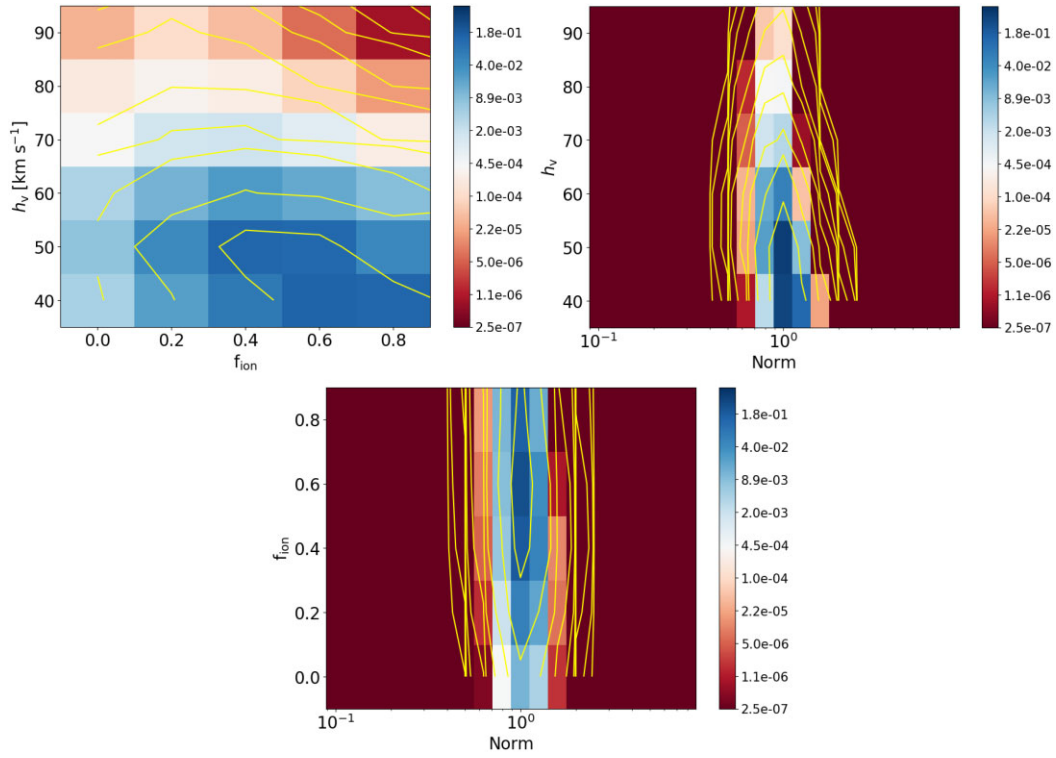


Figure A1. 2D marginalized posterior probability distribution for our pure fountain models onto different 2D spaces: upper left – (h_v , f_{ion}), upper right – (h_v , Norm), and lower-left – (f_{ion} , Norm). Iso-probability contours (in yellow) correspond to 2.51e-07, 1.06e-06, 4.47e-06, 1.88e-05, 7.94e-05, 3.34e-04, 1.41e-03, 5.96e-03, 2.51e-02, and 1.05e-01.

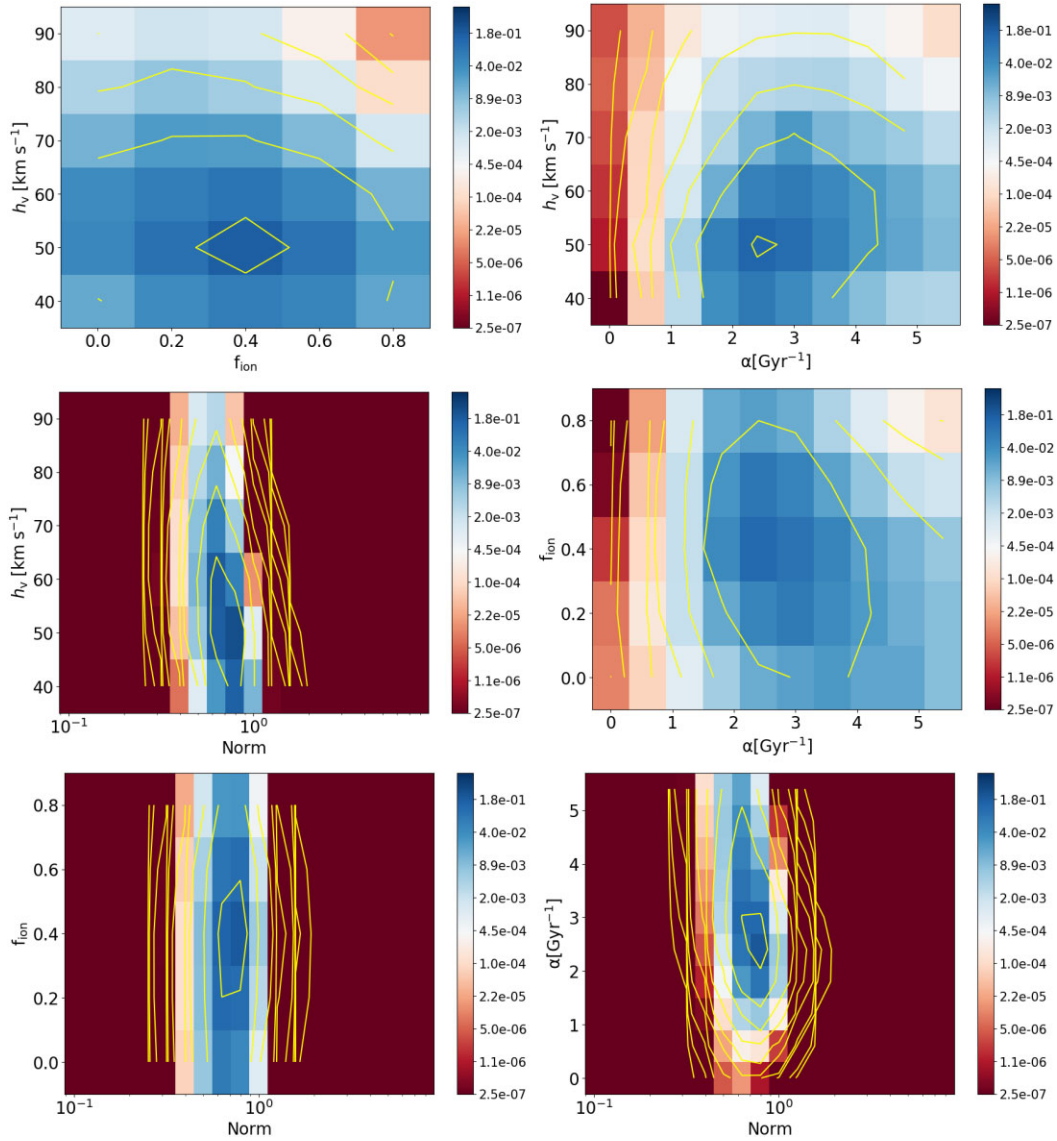


Figure A2. 2D marginalized posterior probability distribution for our fountain + corona accretion models onto different 2D spaces: upper-left – (h_v, f_{ion}) , upper-right – (h_v, α) , middle-left – (h_v, Norm) , middle-right – (f_{ion}, α) , lower-left – (f_{ion}, Norm) , and lower-right – (α, Norm) . Iso-probability contours (in yellow) correspond to 2.51×10^{-7} , 1.06×10^{-6} , 4.47×10^{-6} , 1.88×10^{-5} , 7.94×10^{-5} , 3.34×10^{-4} , 1.41×10^{-3} , 5.96×10^{-3} , 2.51×10^{-2} , and 1.05×10^{-1} .

This paper has been typeset from a $\text{\TeX}/\text{\LaTeX}$ file prepared by the author.